Annals of Biomedical Engineering
https://doi.org/10.1007/s10439-024-03620-y

BMES BIOMEDICAL ENGINEERING SOCIETY

ORIGINAL ARTICLE

Rheological and Lipid Characterization of Minipig and Human Skin Tissue: A Comparative Study Across Different Locations and Depths

Harsa Mitra[1] · Evelyn Nonamaker[2] · Ria D. Corder[1,3,4] · Luis Solorio[2] · Arezoo M. Ardekani[1]

Received: 26 February 2024 / Accepted: 9 September 2024

Abstract

Understanding the rheology of minipig and human skin is crucial for enhancing drug delivery methods, particularly for injections. Despite many studies on skin's viscoelasticity, especially the subcutaneous layer, comparative analyses across different clinical sites are scarce, as is data on the impact of hydration or lipid levels. This study employs shear rheology and lipid analysis to evaluate viscoelasticity and lipid content across three anatomical locations—breast, belly, and neck and three different depth layers in Yucatan minipigs. It reports on how viscoelastic properties change with frequency, time, and strain, noting strain-stiffening and shear-thinning at high strain amplitudes. Human male and female abdominal tissues are also compared to minipig tissues, highlighting distinct viscoelastic traits and lipid's role in them. The findings suggest the existence of species, anatomical location, tissue depth, and sex-based rheological differences. Furthermore, the use of male minipig models for studying human male subcutaneous tissue is discussed.

Keywords Shear rheology · Lipid content · Skin tissue · Subcutaneous

Introduction

Biotherapeutics have emerged as a popular class of drugs due to their potential to treat a wide range of diseases. Among the various routes of administration, subcutaneous (SC) delivery is often preferred due to its convenience, leading to improved patient compliance and reduced healthcare costs [1–5]. However, the translation of these therapies into clinical use is often hindered by physiological barriers [4, 6, 7]. Specifically, the mechanical properties of the subcutaneous space, including its viscoelasticity, can limit the volume of the drug that can be administered and its subsequent dispersion and absorption [3, 8–13]. As minipigs provide strong clinical relevance to humans, minipig SC-adipose tissue models have been increasingly used to study pharmacokinetics of various biopharmaceutical injection therapies, especially through the SC route [14]. Therefore, understanding the mechanistic, rheological, and biochemical relationships between minipig models and humans is essential.

The lipid content of the different layers of skin tissue, including the dermis, SC tissue, and hypodermis, can affect the viscoelasticity of the skin, and in turn, the success of SC injections [15, 16]. Higher levels of lipids could result in a more compliant dermis, while lower levels can be associated with a stiffer dermis [17, 18]. A stiffer dermis increases the resistance of the skin to needle penetration, affecting drug transport and distribution and potentially leading to injection errors or discomfort for the patient [8, 10–12]. The needle length and the hypodermis (SC thickness) impact the drug distribution [15, 19, 20]. Additionally, studies have shown correlations between lipid content/water retention and tissue viscoelasticity [16, 21–23]. Lozano et al. showed water content contributes to the altered mechanics in collagen-rich soft tissues [21]. Although experimental techniques have been previously used

Associate Editor Estefanía Peña oversaw review of this article.

✉ Arezoo M. Ardekani
ardekani@purdue.edu

[1] School of Mechanical Engineering, Purdue University, 585 Purdue Mall, West Lafayette, IN 47907, USA

[2] Weldon School of Biomedical Engineering, Purdue University, 206 S Martin Jischke Dr., West Lafayette, IN 47907, USA

[3] School of Materials Engineering, Purdue University, 701 W Stadium Ave., West Lafayette, IN 47907, USA

[4] Present Address: Department of Chemical and Biomolecular Engineering, University of Tennessee, 1512 Middle Drive, Knoxville, TN 37996, USA

Published online: 18 September 2024

to understand biomechanical behavior, the shear rheology research in this area is limited.

In shear rheology, we have two regimes. The first is the linear viscoelastic (LVE) regime. In LVE, tissue deformation and applied stress are linear and governed by a time-dependent convolution integral, making the response history-dependent. In contrast, non-linear viscoelasticity occurs outside this range (at large-strain amplitudes), where tissue response is no longer proportional to stress, often irreversible, and dependent on the magnitude and rate of applied stress. Such non-linearities expose the intra/intercycle processes that the material is undertaking. Malhotra et al., under small amplitude oscillatory shear (SAOS), showed skin elasticity is determined more by the epidermis and body location than by age, directing toward the importance of understanding location-dependent viscoelasticity [24]. Pan et al. concluded male human skin exhibited strain-stiffening and shear-thinning behavior under large amplitude oscillatory shear (LAOS) [25]. We will discuss such shear-dependent intra-cycle non-linear behavior in detail in "Rheological Methodology and Modeling" section. The degree of strain-stiffening was reported to be age-dependent. Sun et al. reported minipig adipose tissues were stiffer than the human abdominal adipose tissue under compression and simple shear [26]. Geerlings et al. probed the viscoelasticity and described the power-law behavior of the SC-adipose tissue [27]. These studies provide evidence of the variations in the biomechanical/viscoelastic properties of human cadaver skin at different locations.

The current study aims to quantify, compare, and describe the dependence of the tissue viscoelasticity based on its total lipid content. We compare three different anatomical locations, i.e., breast, belly, and neck, in a male Yucatan minipig at three different skin-tissue layers. SAOS and LAOS bulk rheology and the Bligh–Dyer method of lipid isolation are used to evaluate the viscoelasticity and lipid content, respectively, across minipig and human skin tissues. An additional case of human belly SC (male and female) is included for comparison purposes. We use the power-law and the four-element Maxwell models to extract the various parameters from the frequency and stress relaxation tests. These values can be used for modeling the viscoelastic behavior of various layers at different anatomical locations and will lead to advancing tailored injection techniques for patients. This would improve the overall efficacy of drug delivery through the SC route, minimizing patient discomfort and treatment-related complications.

Materials and Methods

Tissue Extraction

Tissue collection was conducted in accordance with an approved protocol (# 2011002085) from the Purdue University Institutional Animal Care and Use Committee (IACUC). One male Yucatan minipig that had been castrated before 3 months of age and weighed about 40 pounds was used in the experiments. The minipigs were sedated by Purdue University veterinary staff, and the areas of interest (breast, belly, and neck) were shaved. A sterile scrub was then performed, repeated three times with alternating washes of chlorhexidine and sterile gauze. Subsequently, the minipigs were euthanized, and a postmortem scrub was performed, following the same sterile scrub procedure. Tissues from the areas of interest were then extracted using sterile surgical tools and collected in clean plastic bags, which were stored at − 80 °C. Two Caucasian human abdominal SC samples, one male (27-year-old with BMI 26.5) and one female (43-year-old with BMI 31.1), were received from GenoSkin Inc. (MA, USA). Both had a Fitzpatrick skin type classification of two. All the tissue samples were placed in clean 2-mL tubes, snap frozen, and stored at − 80 °C.

Rheological Methodology and Modeling

To probe the viscoelastic behavior of the tissue samples, bulk rheological tests were performed on a Discovery Hybrid Rheometer (DHR) 2 (TA Instruments, DE, USA). The 8 mm stainless-steel sandblasted flat-plate geometry was used along with the Peltier Plate Immersion Cell. The setup is shown in Fig. 1D. The rheological properties of tissues vary with the number of freeze-thaw cycles [28–31]. As reported by Corder et al., 27% reduction in storage modulus was observed between the first and second free-thaw cycle [28]. Hence, we employed only one freeze-thaw cycle before the tests were performed. The tissue extraction was performed using a 16 mm diameter arch punch from the belly, neck, and breast (see Fig. 1A). This 16-mm chunk is extracted about 15 min of incubation in room temperature. In this state, the tissues were still stiff and easy to punch out and prepare the final sample disks. The resulting biopsy from these punches was then sliced using a scalpel to create the three layers (approx. 2.4 mm thick). Next, to fit the rheometer geometry, three 8-mm-diameter disks were extracted from each layer using a biopsy punch for triplicate measurements (see Fig. 1C). This process was repeated for each of the minipig locations and the male and female human specimens. It is important to note, that during the 16 mm punching process, the tissue disk stretches and increases the

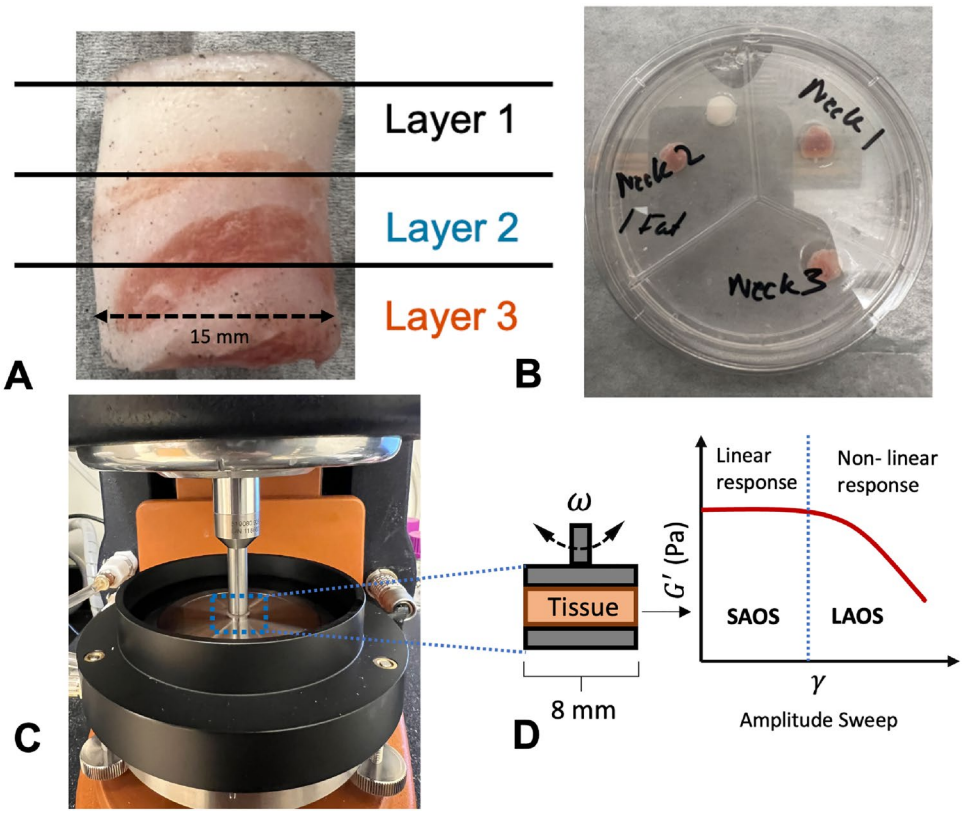

Fig. 1 Tissue sample extraction for the rheological tests represented for the minipig neck tissue. **A** Punched out tissue with the lines representing the approximated thickness of each layer. Layer 1 excludes the epidermis for all the samples. **B** Top view of the sliced layer 1 for the minipig neck tissue. **C** DHR-2 Rheometer with the 8-mm parallel-plate geometry and the immersion cell. **D** Schematic of the oscillatory shear rheology technique. The amplitude sweep graph schematic shows the difference between the linear (SAOS) and non-linear (LAOS) responses

planar dimension of the tissues. While one disk of the triplicate was being tested, other two 8-mm disks were stored in the fridge at 4 °C until the rheological testing. Meanwhile, the two other 16-mm disks were stored at − 80 °C instantly after slicing to minimize the effects of freeze-thaw. The triplicates are averaged, considering the intra-layer biochemical variations and the effects of storage at 4 °C for the two other 8-mm samples. Once extracted, the 8-mm disk samples were allowed to equilibrate at 37 °C for 15 min in a petri dish while immersed in 7.4 pH phosphate-buffered saline (PBS) (Gibco, NY, USA). After equilibration, the samples were loaded onto the rheometer geometry and the tests were run at a fixed 2 mm gap (16% compression). The axial force at the start of the experiment was always between 0.16 and 0.25 N. The samples are placed in a top-down manner, i.e., the flat surface closest to the epidermis of each 8-mm disk, is in contact with the moving plate of the rheometer. Fixing a constant gap height has been shown to produce more consistent results as compared to varying the gap based on the sample thickness [28]. After the sample was loaded and fixed firmly between the plates, 45 mL of PBS 7.4 pH buffer was poured into the immersion cell to avoid sample drying over the period of each test.

To evaluate the rheological properties of the samples, G' (storage) and G'' (loss) moduli were measured as a function of frequency and strain amplitude. The frequency sweep at strain amplitude (γ) of 0.5% and angular frequency (ω) range of 0.04–40 rad/s, and amplitude sweep at ω =1 rad/s and $\gamma \in [0.01-40\%]$ was performed. A power-law relation is fitted to the linear storage moduli as a function of frequency as

$$G' = G_0 \omega^p, \tag{1}$$

where G_0, and, p are constants [27, 32, 33]. For the relaxation tests (at 40% strain), the relaxation modulus, $G(t)$, is fit to the four-element generalized-Maxwell (GM), also known as Maxwell–Wiechert model, and can be described by the following equation [34],

$$\left.\begin{array}{c} \sigma = \gamma_0 \sum_{i=1}^{n} E_i exp(-t/\lambda_i), \\ E_i = \frac{\eta_i}{\lambda_i}, \end{array}\right\}, \tag{2}$$

where σ, γ_0, η_i, and λ_i are the total stress response, constant applied strain at $t = 0$, viscosity, and relaxation time of the of the ith Maxwell element, respectively. The GM model parameters can be utilized to calculate the frequency-dependent storage and loss moduli. It should be noted that this applies only for the linear regime, they do not hold for the non-linear regime (LAOS). Therefore, for the linear regime, frequency-dependent moduli can be defined as follows [34]:

$$\left.\begin{aligned} G'(\omega) &= \sum \frac{\eta_i \omega^2 \lambda_i}{1+\omega^2 \lambda_i^2}, \\ G''(\omega) &= \sum \frac{\eta_i \omega \lambda_i}{1+\omega^2 \lambda_i^2}. \end{aligned}\right\} \tag{3}$$

To quantify the non-linear (LAOS) response of the tissues, the stress response waveforms were recorded for each strain amplitude during the strain sweep [28, 29].

The shear stress response can be described as a sum of higher harmonic contributions as [35, 36]

$$\tau(t) = \sum_{n-\text{odd}} \tau_n \sin(n\omega t + \delta_n) = \sum_{n-\text{odd}} \gamma_1 |G_n^*| \sin(n\omega t + \delta_n), \tag{4}$$

where $|G_n^*| = \sqrt{G'^2_n + G''^2_n}$ is the scaled stress magnitude and should not be confused with the complex modulus. G'_n, and G''_n are the Fourier coefficients (time domain) relating the elastic/viscous Chebyshev coefficients in the strain/strain-rate domain, respectively (For details see [36]). Also, γ_1, and δ_n are the maximum applied strain and the phase variable that determines the initial conditions of the higher-harmonics. Using the framework described by Ewoldt et al., intra-cycle non-linearities, strain-stiffening/softening, and shear-thinning/thickening behavior can be quantified using the following set of variables [35]. The periodic stress response at a steady state is plotted parametrically against the strain response. Such representations are called Lissajous–Bowditch (LB) plots. Material properties can then be determined graphically using the LB plots. In which τ, i.e., total-shear stress, is plotted as a function of γ for the elastic behavior. Whereas the same is plotted as a function of $\dot{\gamma}$ for the viscous behavior. The minimum strain elastic shear modulus or tangent modulus is evaluated at $\gamma = 0, G'_M$. While the large-strain elastic shear modulus is quantified at the maximum imposed strain ($\gamma = \gamma_1$), G'_L. This framework can be understood using the following parameters for a sinusoidal stress/strain input,

$$G'_M = \frac{\mathrm{d}\tau}{\mathrm{d}\gamma}_{\gamma=0} = \sum_{n-\text{odd}} nG'_n \tag{5}$$

and

$$G'_L = \frac{\tau}{\gamma}_{\gamma=\pm\gamma_1} = \sum_{n-\text{odd}} G'_n(-1)^{(n-1)/2}, \tag{6}$$

Similar properties can be quantified for viscous components using the Fourier parameters of the higher harmonic stress contributions. The minimum-rate and large-rate dynamic viscosities, η'_M and η'_L, respectively, can be defined as following [35, 36],

$$\eta'_M = \frac{\mathrm{d}\tau}{\mathrm{d}\dot{\gamma}}_{\dot{\gamma}=0} = \frac{1}{\omega} \sum_{n-\text{odd}} nG''_n(-1)^{(n-1)/2}, \tag{7}$$

and

$$\eta'_L = \frac{\tau}{\dot{\gamma}}_{\dot{\gamma}=\pm\dot{\gamma}_1} = \frac{1}{\omega} \sum_{n-\text{odd}} G''_n \tag{8}$$

where $\dot{\gamma}$ is the shear-rate. Based on these sets of variables, a strain-stiffening ratio is defined as [35]:

$$S(\omega, \gamma_1) = \frac{G'_L - G'_M}{G'_L}, \tag{9}$$

and the shear-thickening ratio

$$T(\omega, \gamma_1) = \frac{\eta'_L - \eta'_M}{\eta'_L}. \tag{10}$$

For cases when $S > 0$, the elastic behavior of the material can be interpreted as intra-cycle strain-stiffening, whereas $S < 0$ indicates intra-cycle strain-softening, $S = 0$ for a linear elastic response. The S parameter becomes crucial in understanding tissue functionality, as it relates to how tissues maintain structural integrity or adapt under physiological stresses. Similar to the elastic behavior, the viscous counterpart $T > 0$ corresponds to intra-cycle shear-thickening and $T < 0$ indicates intra-cycle shear-thinning. Also, it is to be noted that, $T = 0$ corresponds to a linear viscous response [35]. In simpler terms, the T parameter describes the tissue's ability to change under deformation at different shear rates. This is vital to quantify tissue fluidity and its response to dynamic loading. In summary, a high positive S value combined with a higher magnitude of T (when $T < 0$) results in a higher degree of stiffening as strain is applied. But also accompanies a faster dissipation of the developed non-linear elastic stresses through the shear-thinning behavior of the tissue. All the tests were carried out in a triplicate manner and at 37 °C while immersed in 45 mL of PBS (pH 7.4).

Lipid Quantification

After rheology testing, the total lipid content of each human and minipig tissue sample was quantified using the following approach based on the Bligh–Dyer method of lipid isolation [37]. It is noteworthy that there may be lipid loss (as the samples were submerged in PBS solution) during the course of the rheological tests due to shearing. Hence, the measured quantities could differ from the initial lipid contents in the samples before each test. To allow for repeated measurements of lipid content at each layer, the individual tissue disks from rheology (e.g., Neck Layer 1, Belly Layer 2, etc.) were divided into three samples of equal tissue mass. These smaller samples were then homogenized in 200 µL of 8 M urea (Sigma Aldrich, MO, USA) using the Qiagen TissueRuptor (Quiagen N.V., Germany). To

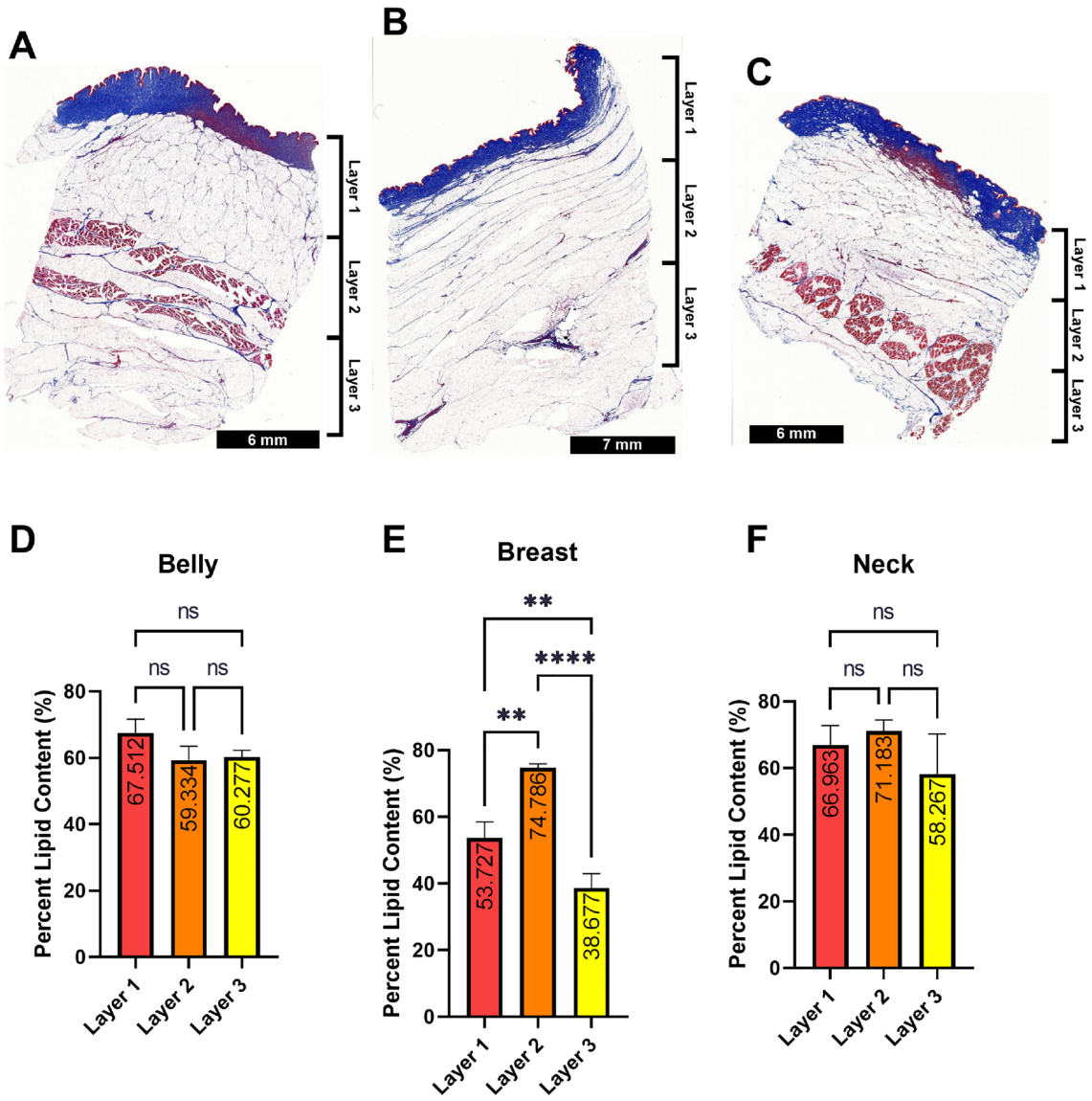

Fig. 2 Comparison of percent lipid content across minipig anatomical locations. **A** Masson's trichrome stain of minipig belly tissue. **B** Masson's trichrome stain of minipig breast tissue. **C** Masson's trichrome stain of minipig neck tissue. In **A**, **B**, **D**, tissue regions rich with, collagen appear blue, muscle appears red, and cellular cytoplasm appears light pink. **D** Percent lipid content of tissue layers obtained from the minipig belly region, post-rheology testing. **E** Percent lipid content of tissue layers obtained from the minipig breast region, post-rheology testing. **F** Percent lipid content of tissue layers obtained from the minipig neck region, post-rheology testing. Data in **D**–**F** are reported as the mean ± SD of nine 20 mg samples resulting in no significance (ns) or p values ($**p \leq 0.01$, $****p \leq 0.0001$)

these tissue homogenates, 800 µL of methanol (Acros Organics, Belgium), 400 µL of chloroform (Sigma Aldrich, MO, USA), and 300 µL of Milli-Q water (Millipore Sigma, MA, USA) were added with vortexing between reagent additions. Samples were then centrifuged at 7000×g for 5 min to allow hydrophobic separation to occur. After centrifugation, the upper soluble layer was aspirated, leaving the bottom insoluble layer containing a mixture of lipids and chloroform. The insoluble layer of each sample was then transferred into a clean 0.5 mL tube and placed in the CentriVap Benchtop Vacuum Concentrator (Labconco, MO, USA) at 45 °C for 8 h to evaporate the remaining chloroform. The total lipid mass for each sample was calculated to be the mass of the dried insoluble pellet. The percent lipid content was calculated to be the ratio of the total lipid mass to the mass of the dissected tissue sample. Statistical analysis between groups was completed using a one-way ANOVA with Tukey comparisons. To visualize tissue composition, histological analysis using a Masson's trichrome stain was performed on representative cross-sections of tissue from

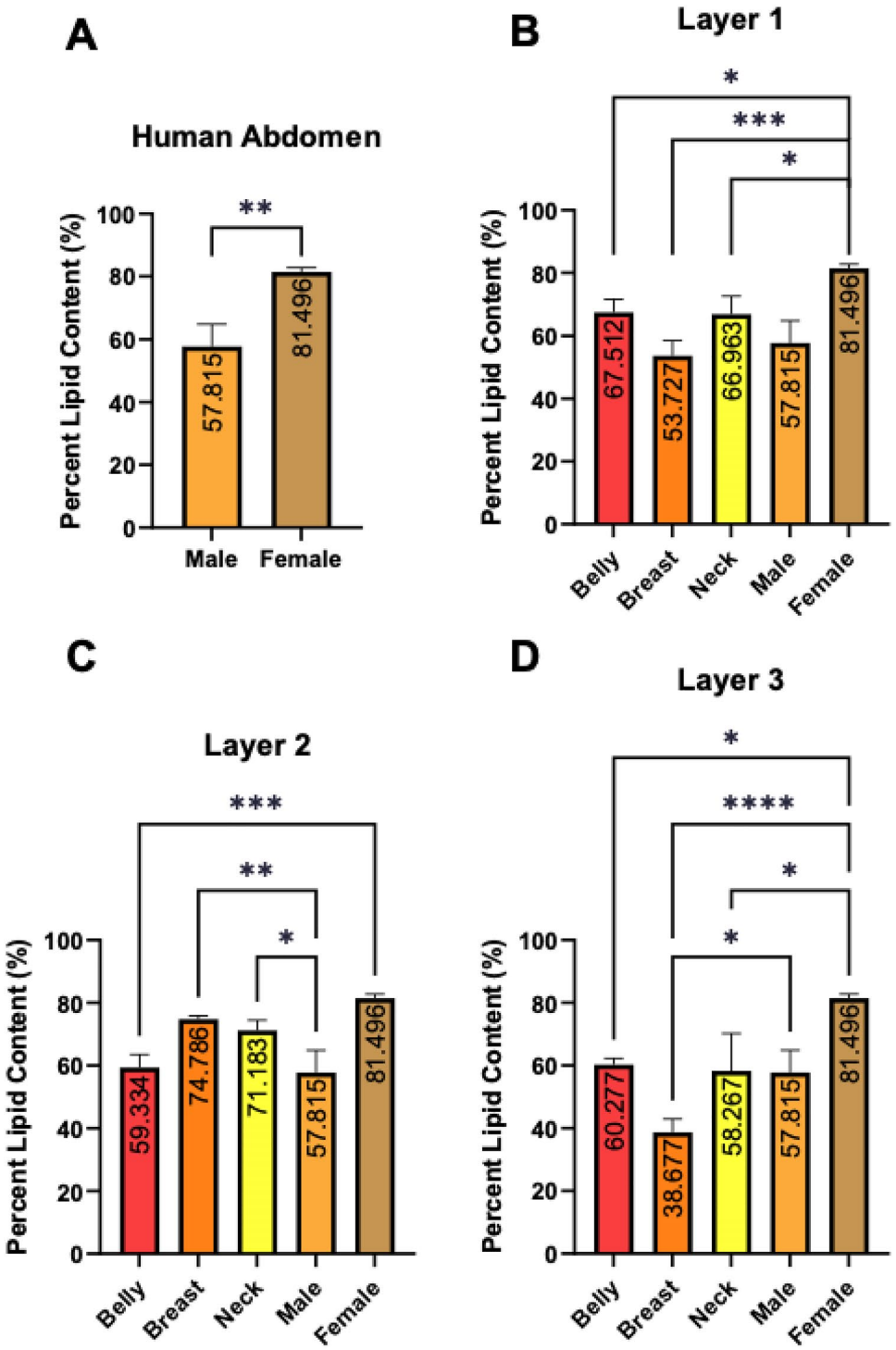

Fig. 3 Comparison of percent lipid content between human and minipig tissues. **A** Percent lipid content of human tissue samples isolated from GenoSkin models. **B** Comparison of percent lipid content between human samples and layer 1 of all minipig anatomical locations. **C** Comparison of percent lipid content between human samples and layer 2 of all minipig anatomical locations. **D** Comparison of percent lipid content between human samples and layer 3 of all minipig anatomical locations. Data in **B–D** are reported as the mean ± SD of nine 20 mg samples resulting in no significance (ns) or *p* values (* $p \leq 0.05$, ** $p \leq 0.01$, *** $p \leq 0.001$, **** $p \leq 0.0001$)

each of the three minipig anatomical locations. This was done to illustrate the differences in tissue structure across the layers and to understand the depths of the different layers. In this analysis, tissues rich in collagen appear blue, muscle tissue appears red, and cellular cytoplasm appears light pink.

Results

The mass fractions of the lipid contents are presented along with the rheological evaluation of the minipig and human skin tissues.

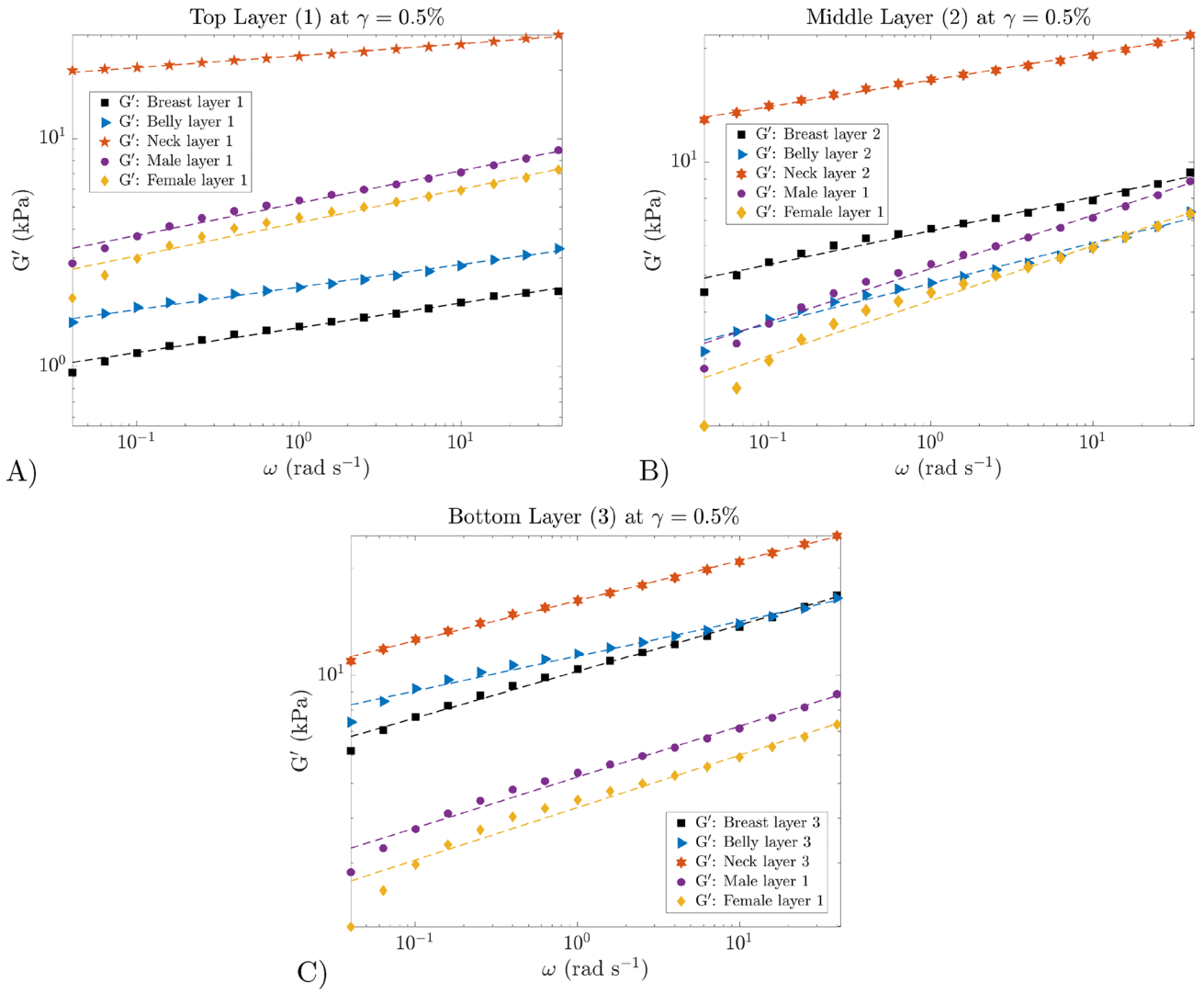

Fig. 4 Storage modulus, $G'(\omega)$, for the three different regions of the minipig, i.e., breast, belly, and neck, across the different layers, 1–3, represented through **A**–**C**, respectively. Dashed lines present the power-law fit. The male and female human SC samples are overlaid in all the figures for comparison. Manual scaling has been done for, $G'(\gamma)$, across **A**, **B**, and **C**, to make the breast, belly, and neck layers' magnitude differences decipherable. Standard deviations were about the size of the symbols

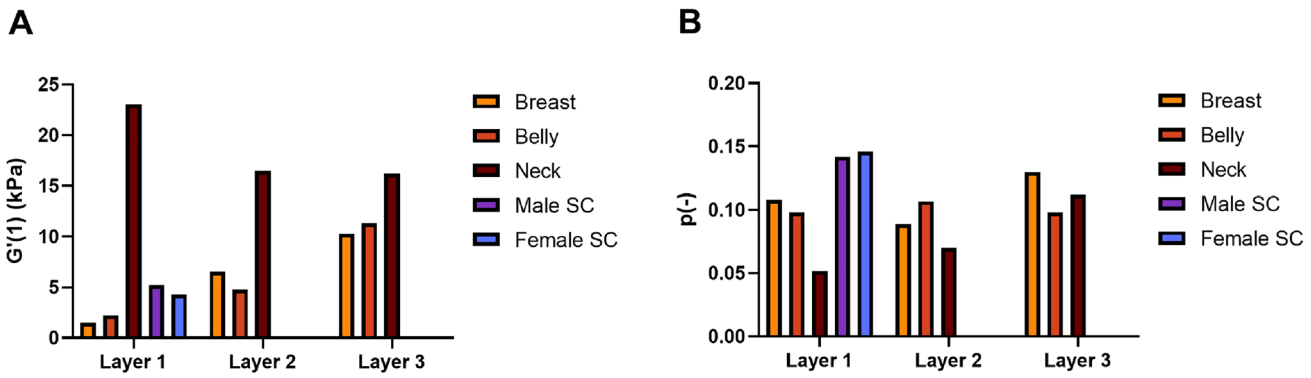

Fig. 5 Visualization of the fitted parameters for the frequency sweep data in Table 1. **A** $G'(1)$, and **B** p, for all the layers and locations are displayed. The male human/female SC fits are represented with the minipig layer 1 for both parameters for comparison

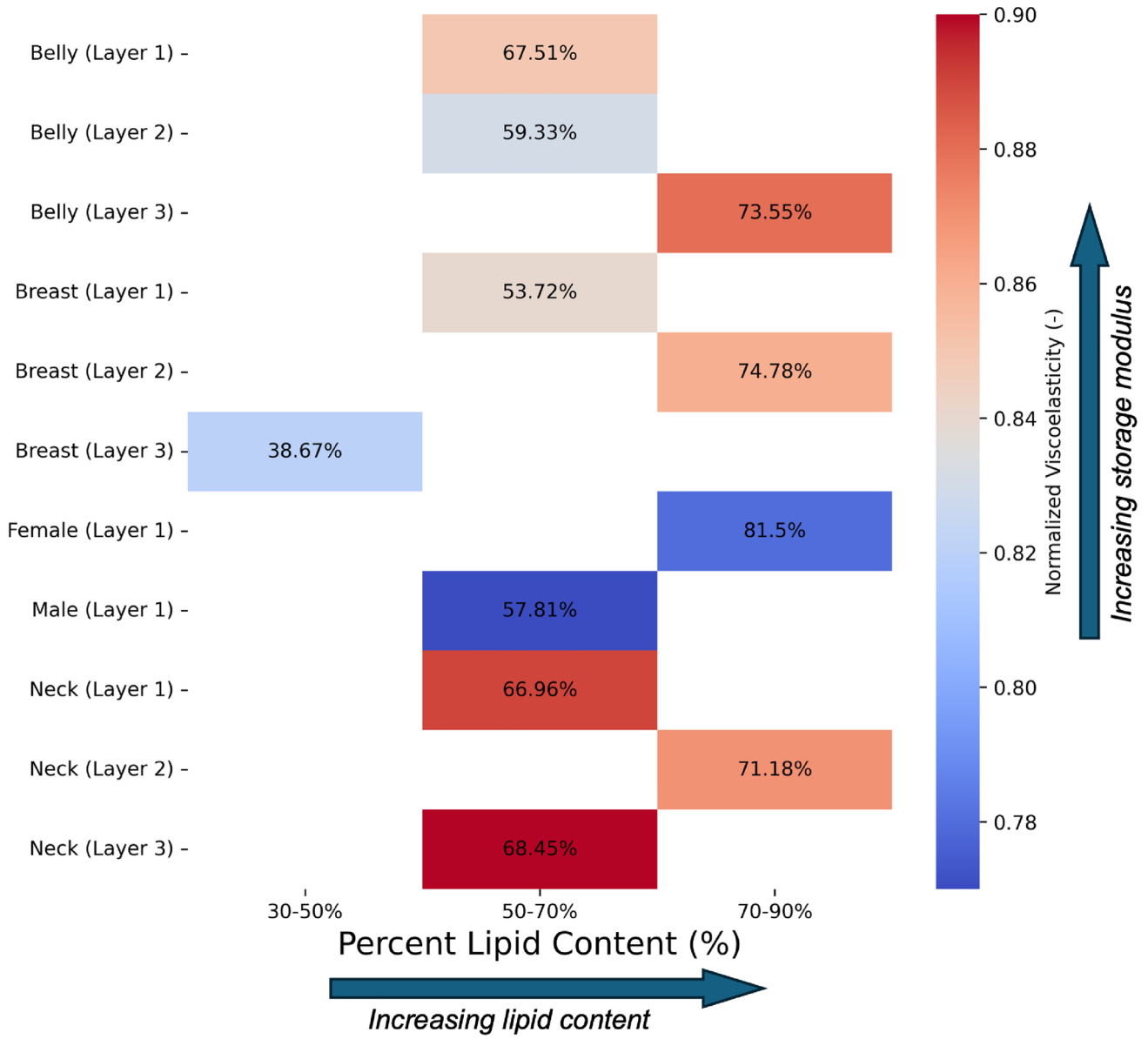

Fig. 6 A colored heat map of the normalized viscoelasticity at $\omega = 1$ rad/s, i.e., purely viscous/elastic at a value of zero/one, w.r.t. percent lipid content. Additionally, each viscoelastic value for the respective tissue is overlaid with the corresponding percent lipid content. The female and male layer 1 represents the human SCs. A correlation of $r = 0.73, p = 0.024$ is observed among all the minipig tissue viscoelasticity and the lipid content

Histology and Lipid Contents

Histological examination revealed similar tissue morphologies across the minipig belly and neck cross-sections (Fig. 2A, C). Both tissues contained largely clear striations of the dermis, SC, and muscle tissue, indicated by the regions stained predominantly blue, white, and red, respectively. However, the minipig breast tissue was observed to have larger white adipose deposits throughout, clusters of blue collagen surrounding mammary glands near the center of the tissue, and no clear muscle layers (Fig. 2B). Collagen content was additionally quantified for the SC layers (layer 1) for the belly, breast, and neck regions. Liquid chromatography-tandem mass spectrometry (LC-MS/MS), a commonly used protein identification technique, was employed [38]. The tissues were then measured and determined to comprise $92.9 \pm 3.19\%$ of the total matrix protein in the neck region, $89.9 \pm 2.83\%$ of the total matrix protein in the belly region, and $88.3 \pm 5.48\%$ of the total matrix protein in the breast region.

The minipig belly and neck tissues also behaved similarly regarding their lipid quantification. In both tissues, the total

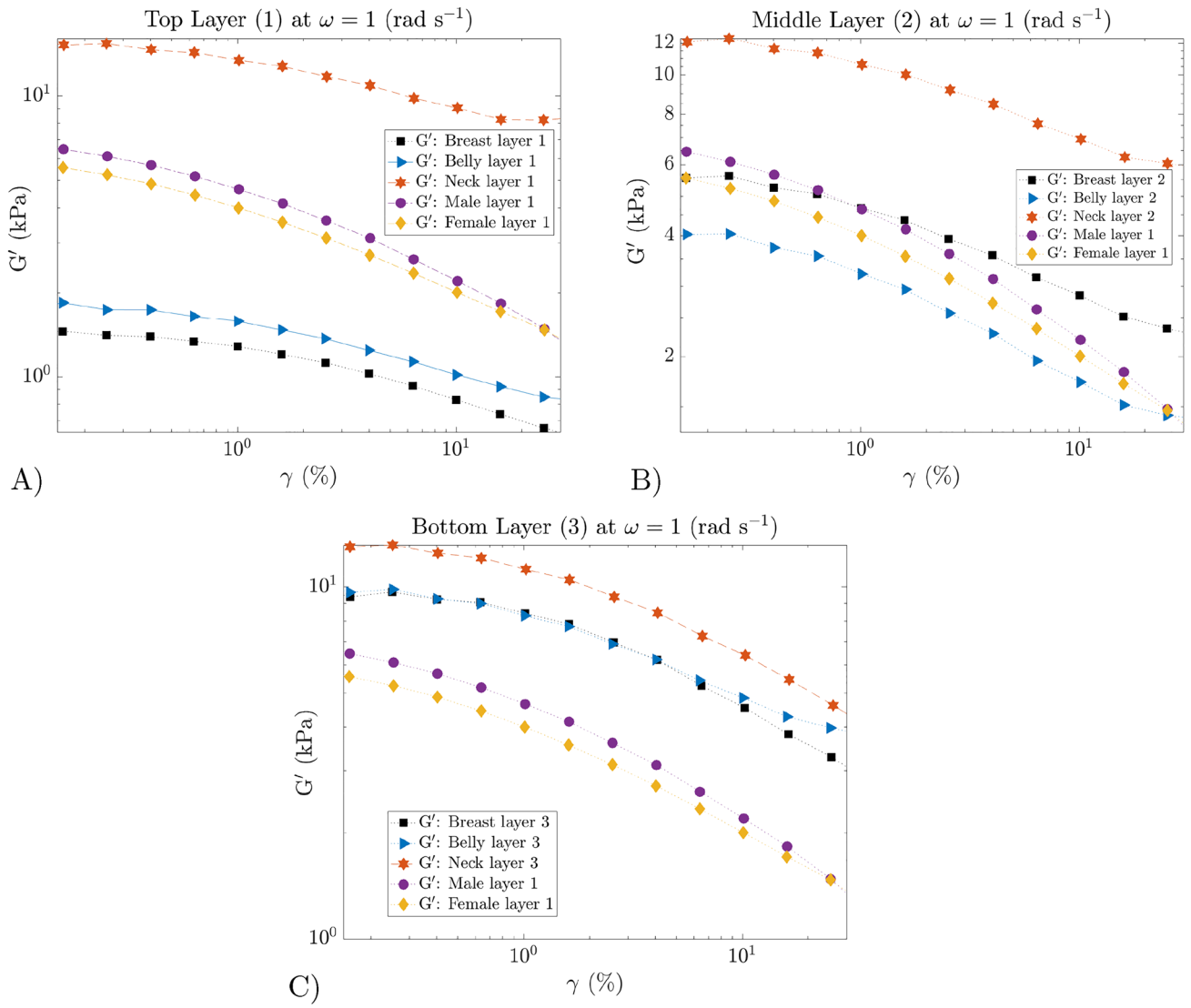

Fig. 7 Storage modulus, $G'(\gamma)$, for the three different regions of the minipig, i.e., breast, belly, and neck, across the different layers, 1–3, represented through **A–C**, respectively. The male and female human SC samples are overlaid in all the figures for comparison. Manual scaling has been done for, $G'(\gamma)$, across **A**, **B**, and **C**, to make the breast, belly, and neck layers' magnitude differences decipherable. An average variation of 16.5% was observed between the three triplicates. Solid lines are overlaid to guide the reader and are not a fit

lipid content remained relatively constant across each of the three tissue depths, at about 60–65% of the total sample mass after rheological testing (Fig. 2D, F). On the other hand, lipid analysis of the minipig breast samples indicated significantly different quantities of lipid across tissue depths. Layer 2, corresponding to the middle 2 mm of the original tissue biopsy punch, had the highest total lipid content at approximately 75% of the sample mass post-rheology testing, whereas layers 1 and 3 contained only 54% and 39% lipid mass, respectively (Fig. 2E).

Upon analyzing the lipid content of the human samples, it was discovered that the female samples contained about 20% more lipids than the male samples (Fig. 3A). Both the male human and female data were compared to the minipig data to determine which minipig anatomical region and depth best correlated to the human tissues in terms of total lipid content. The lipid content of the male human samples was most similar to that of the minipig belly and neck samples across tissue depths, with the exception of layer 2 of the minipig neck (Fig. 3A, C, D). On the other hand, the lipid content of the human female samples was most similar to the minipig breast and neck tissues in layer 2 with marked statistical differences when compared to all other minipig tissues at all other depths (Fig. 3B–D).

Frequency Sweep Tests

The frequency sweep results are presented in Figs. 4 and 11. Standard deviations were about the size of the symbols. The applied strain amplitude for all the tests was 0.5% (SAOS). Thus, the response is expected to be within the linear viscoelastic (LVE) regime. Across all frequency sweeps, the storage modulus exhibits power-law behavior, with the storage modulus being higher than the loss modulus for all cases. The minipig neck layer 2 and breast layer 1 showed the highest and lowest storage modulus, respectively. Considerable differences were observed for both the G' and G'', in Figs. 4 and 11. In Fig. 4A, i.e., layer 1, the neck region (breast region) shows the highest (lowest) storage modulus. A similar trend, i.e., G' : Neck > Belly > Breast, except for, $\omega > 5\ rad\ s^{-1}$, can be observed for the case of layer 3 in Fig. 4C. Although in Fig. 4B, we observed, i.e., G' : Neck > Breast > Belly. The two human SC samples exhibited close agreement to the minipig belly layer 2 in Fig. 4B. Also, it should be noted, in Fig. 4A, the human SC samples behaved stiffer compared to the minipig belly and breast layer 1. Additionally, all the minipig layer 3 samples had higher storage moduli than the human SC samples (Fig. 4C).

In Fig. 11A–C, the loss modulus for all the minipig layers and locations, along with the male human and female SC layers, has been presented. The female SC showed a lower storage and loss modulus as compared to the male counterpart. We discuss this further in "Stress Relaxation Tests" section. Therefore, tissue layers containing a greater quantity of lipids are likely to demonstrate increased flow and deformation when subjected to shear stress, resulting in a lower storage modulus. However, it is important to note that other factors, such as the degree of saturation of the lipids, also play a role in overall storage and loss modulus [39, 40]. A trend, i.e., G'' : Neck > Belly > Breast, similar to the elastic counterpart is observed for the loss modulus across the minipig layer 1 and 2 (Fig. 11A and B,

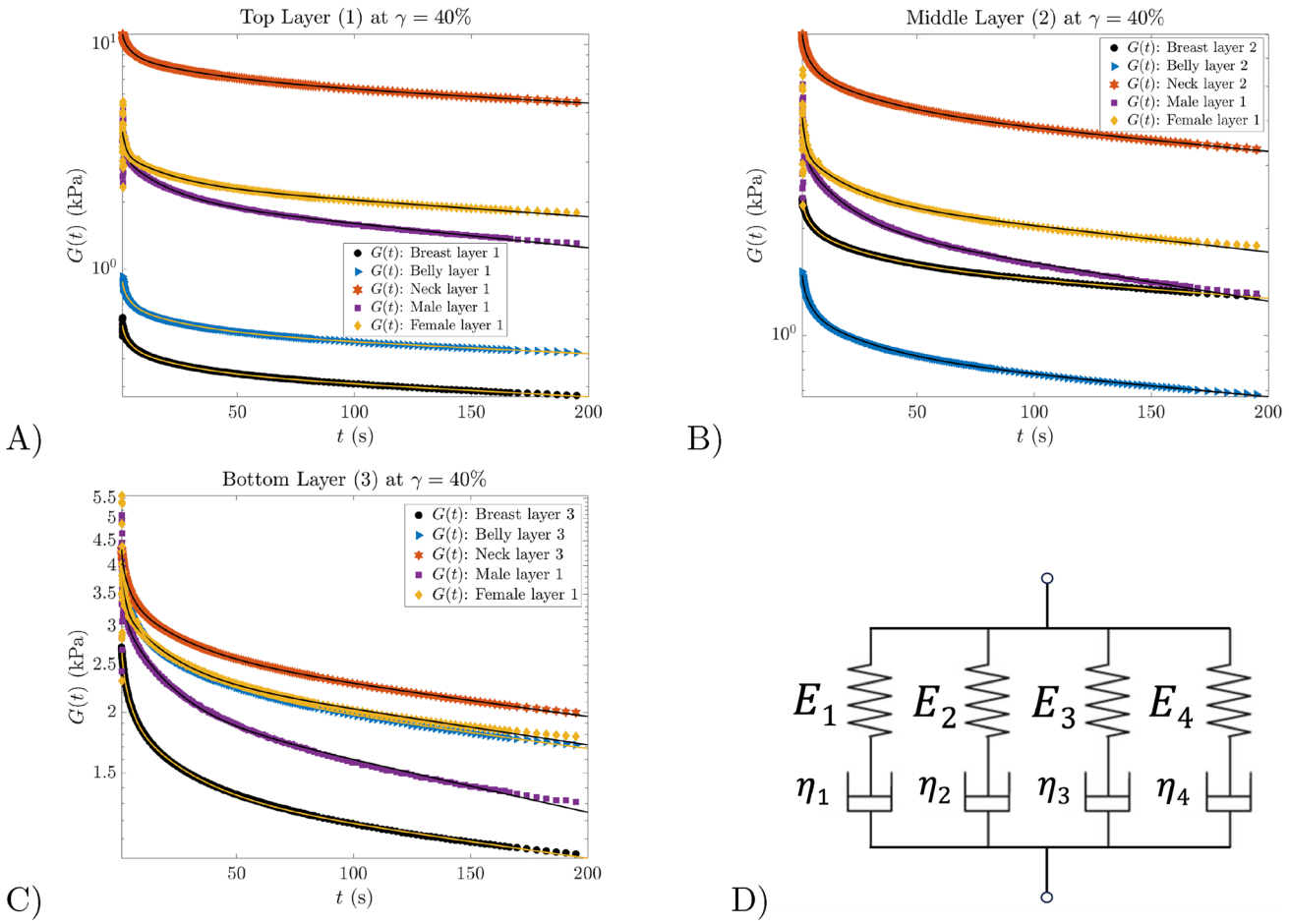

Fig. 8 Relaxation modulus, $G(t)$, for the three different regions of the minipig, i.e., breast, belly, and neck, across the different layers, 1–3, represented through **A**–**c**, respectively. The male and female human SC samples are overlaid in all the figures for comparison. Solid lines represent the four-element GM model fit. The four-element GM model is represented in (**D**). Each arm corresponds to one Maxwell element

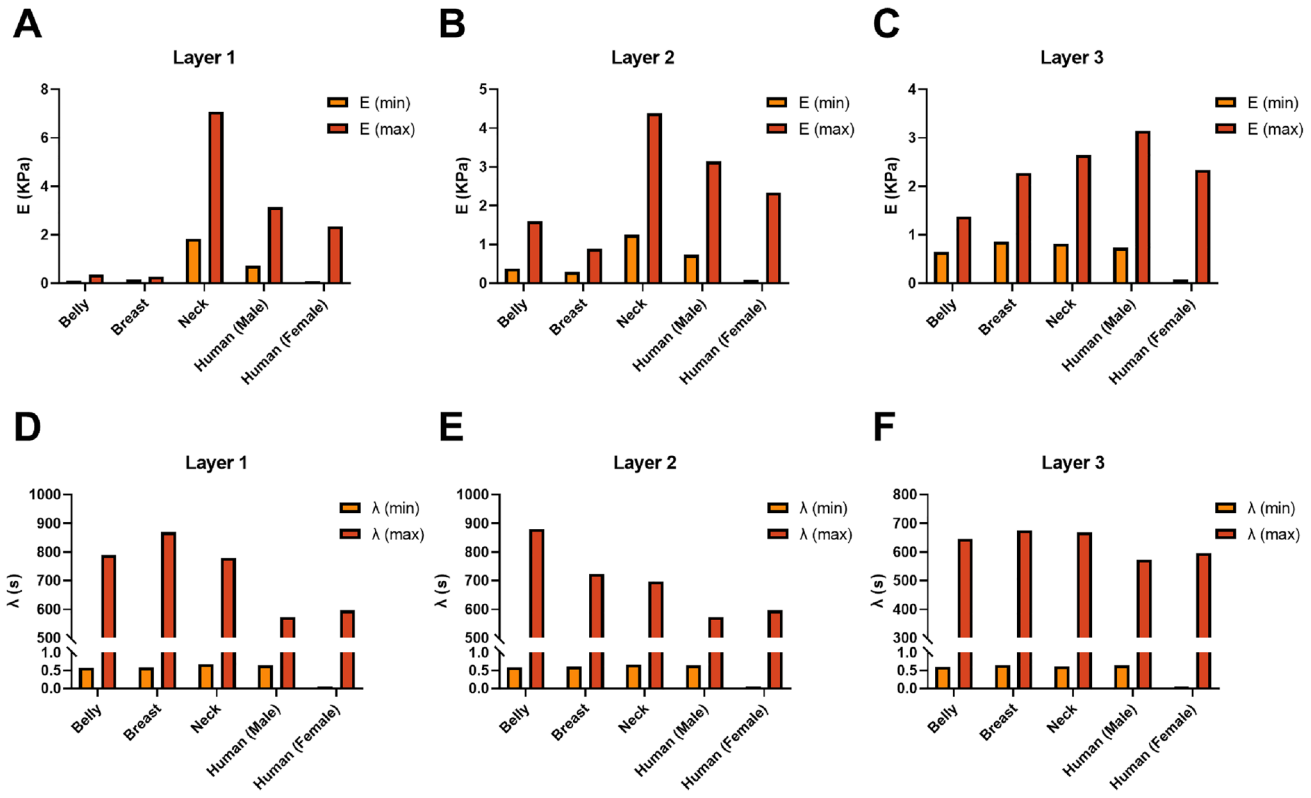

Fig. 9 GM model fit parameters of $G(t)$. The maximum and minimum of the four elements, **A**, **B**, and **C**, represent elastic modulus, E_i, for layers 1, 2, and 3, respectively. **D**, **E**, and **F** show the relaxation time, λ_i, of layers 1, 2, and 3, respectively. The human, i.e., male and female, data are only for the SC (top layer) but is overlaid in all the figures for comparison purposes. It is important to note that the minimum relaxation time values are negligible as compared to their respective maximums. Hence are not visible in (**B**). Table 2 refers to exact values of, E_i, and, λ_i, for all the samples tested

respectively). In terms of the lipid contents in the minipig, belly, breast, and belly possessed the highest fractions in layers 1, 2, and 3, respectively (see Fig. 3B–D), though the neck showed the highest storage modulus in all three layers in Fig. 4. When G' of the belly and breast are compared in Fig. 4, we observe the belly, breast, and belly to have the highest storage modulus, especially at lower frequencies.

The fitted power-law parameters are represented in Fig. 5 and Table 1. In Fig. 5, it can be observed the material with the lowest (highest) $G'(1)$ had the highest (lowest) power index, p. The fitted power-law model with R-square values greater than 0.985 is for all the tested cases (Refer to Table. 1). To further summarize the findings, a normalized viscoelasticity was defined (see Fig. 6) at 1 rad/s. Based on the ANOVA analysis, the minipig tissue storage modulus had a r=0.73 (p=0.024) with the amount of lipid content.

Amplitude Sweep Tests

The averaged storage and loss modulus values from the triplicate tests for all the tissue samples are presented in Figs. 7 and 12, respectively. An average variation of 16.5% was observed between the three triplicates. When compared among each minipig anatomical location, the breast and belly regions showed strong similarities across their $G'(\gamma)$, and $G''(\gamma)$, values among each layer, especially at lower strain amplitudes. Unlike the layers of minipig belly and breast tissue, the three layers from the neck had a narrower range of moduli. Similar to the frequency sweep results for human tissues presented in "Frequency Sweep Tests" section, the female SC (highest lipid content) showed lower storage and loss moduli at lower strain amplitudes as compared to the male counterpart (see Figs. 7 and 12). Also, the storage modulus of both the male human and female SC layers presented a similar behavior to the minipig belly and breast layer 2, as observed in Fig. 7B. Specific to the storage modulus, as seen in Fig. 7, layer 1 compared to layers 2 and 3, showed earlier onset of non-linear viscoelastic response [28, 29, 41, 42].

Comparing the magnitude of $G'(\gamma)$ across the three minipig layers in Fig. 7, we observe a similar trend to the frequency sweep results, as expected and as explained in "Frequency Sweep Tests" section. Based on the

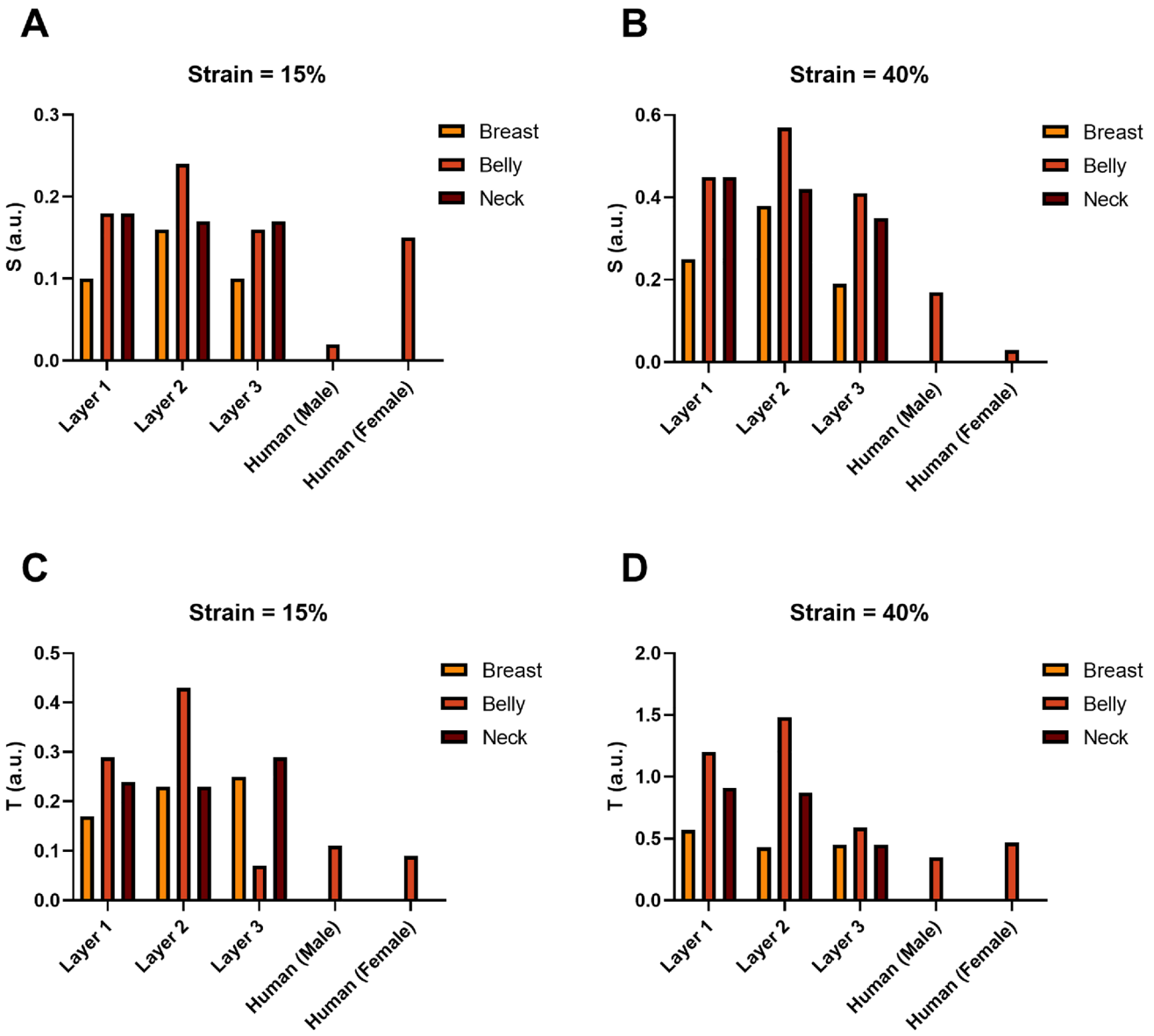

Fig. 10 **A, B** represent the S (elastic behavior) values for both the strain conditions of 15%. and 40%, respectively. **C**, **D** show the T (viscous behavior) values for 15% and 40% applied strain. The respective S and T values are tabulated in Tables 4 and 5

evaluations shown in Figs. 7 and 12, the minipig neck layer 2 and layer 3 showed the highest magnitude of storage and loss modulus, respectively, across $\gamma = 0.01$ to 40%, among all the test cases. The minipig breast layer 1 showed the lowest-magnitude moduli. For the SC layers (layer 1), the minipig breast region had lower moduli as compared to the belly (see Figs. 7A and 12A). Compared to the minipig belly and breast SC tissues, the male human and female SC tissues had higher moduli (see Figs. 7A and 12A).

Additionally, within the linear region, storage and loss moduli are independent of the applied strain amplitude (at a constant frequency). This results in a sinusoidal wave. In the non-linear region, storage and loss moduli are a function of the strain amplitude when the frequency is kept constant. Consequently making the stress waveforms distorted from sinusoidal waves [43]. We will discuss the non-linear response in detail in Sec. 3.5. Using this information, across Figs. 7 and 12, among the lower two layers, i.e., 2 and 3, layer 2 had an earlier onset of non-linearity. A higher degree of non-linearity, especially at higher strain amplitudes, is observed in the human SC tissues, as compared to the minipig cases in Figs. 7 and 12. In brief, close agreement between the minipig belly and breast was observed, especially for layers 1 and 3. Layer 3 showed the highest similarity for all the minipig tissue cases. The minipig neck layers

showed similar storage modulus across the various layers, although the behavior is reduced at higher strain amplitudes.

Stress Relaxation Tests

The relaxation behavior of the tissue samples under a constant application of strain is quantified and represented in Fig. 8. All the tests are performed at a constant shear strain of 40%, specifically probing the non-linear region. Across the triplicate tests, the magnitude of $G(t)$ across the three tests varied at an average of 11%. In this study, we used a four-element GM model, i.e., $n = 4$, which showed the best fit for all the relaxation data (see Fig. 8D). The fitted parameters are tabulated in Table 2. For better comparison, the maximum and minimum elastic modulus and relaxation time, i.e., among the four elements, are presented in Figs. 9A and B, respectively.

Additionally, the relaxation half-life times [44], $\lambda_{1/2}$, i.e., timescale at which the stress is relaxed to half its initial value, are presented in Table 3. A clear difference between the half-times is observed between the minipig and human tissues, with the former exhibiting longer half-lives. A shorter half-life time results in a faster remodeling of the tissue matrix under stress. Moreover, we notice, the neck region's half-life times are relatively similar across the layers, suggesting a more uniform relaxation behavior. The breast location showed the most variability in their half-life times among each layer. In Fig. 8A and C, the magnitude of the relaxation modulus follows the order of $G(t)$: Neck > Belly > Breast. However, between each location, the difference in the magnitude of $G(t)$ is more significant in layer 1 (see Fig. 8A), especially between the neck and belly/breast. In Fig. 8B, the minipig- layer 2, the relaxation modulus magnitude followed the trend of $G(t)$: Neck > Breast > Belly. Additionally, the human SC samples had a closer agreement with the minipig breast layer 2 (see Fig. 8B). Noticeably, the female SC showed the strongest correlation to the belly layer 3, as observed in Fig. 8C. The human female SC layer had a higher degree of relaxation as compared to the other male human SC and minipig layers.

As discussed in previous sections (see "Frequency Sweep Tests" and "Frequency Sweep Tests" sections), tissues/tissue layers with higher lipid content will have a lower storage modulus. This is evident across the male human and female SC in Fig. 9A. Although, in Fig. 9B, the maximum relaxation time for both the male human and female SC tissues were similar, suggesting that a faster stress relaxation behavior is not necessarily accompanied by a higher viscous behavior. Therefore, it is important to note that the relationship between lipid content and stress relaxation can be more complex and could depend on other factors not quantified here. However, the neck has the highest elastic modulus (see Fig. 9A.i, ii, and iii). As seen in Fig. 9B.i and ii, the belly and breast in layers 1 and 2 showed the longest relaxation times. All the minipig layers showed similar relaxation times in layer 3 (see Fig. 9B.iii). In brief, the relaxation behavior of the tissues followed a four-element GM model. In comparison to all the tissue cases, the male human SC showed the fastest relaxation. This can be observed from the fast relaxation times for the male and female human SC in Fig. 9B.i, ii, and iii.

LAOS Tests

The recorded strain waveforms at each strain amplitude during the amplitude sweep tests were post-processed using MITLaos [36]. The S and T parameters are quantified for all the tissue samples at strain amplitudes of 15 and 40%. All the results shown are at $n = 3$ and $\omega = 1$ rad s^{-1}.

For brevity, only the S and T values for $\gamma = 15\%$ and 40% are visualized in Fig. 10 and also tabulated in Tables 4 and 5. Additionally, the LB plots are presented for all the tissue cases in Fig. 13. All of the tissues from both the minipig and human skin showed strain-stiffening and shear-thinning behavior. This can be observed from the S and T values in Tables 4 and 5. It should be noted the non-linear behavior is sensitive to the testing conditions, such as compression and pre-straining. Previous observations of strain-softening and strain thinning in tissues have been also reported [25, 45, 46]. As compared to the human SC layers, higher values of S and T are observed for the minipig tissue layers, especially at the higher strain amplitude of 40%. Except for the elastic behavior of the female SC. In conclusion, all the tissue cases showed strain-stiffening and shear-thinning behavior. The female SC tissue with the highest lipid content (81.49%) showed the lowest degree of strain-stiffening behavior with, $S = 0.03$ and $S = 0.15$, for 40% and 15% strain, respectively, accompanied by an increased strain amplitude. However, the female SC showed an increase in the shear-thinning degree, compared to the rest of the tissue cases. This can be explained by the negative correlation between lipid content and stiffness [17]. Apart from the female SC, all the tissues showed a higher degree of strain-stiffening behavior at higher strain amplitude (see Tables 4 and 5).

Discussion

The biochemical composition of tissue, namely its lipid content, plays a role in driving its viscoelastic properties via hydrophobic interactions. To explore this hypothesis, we extracted the total lipid content of minipig tissue samples isolated from the belly, breast, and neck region of castrated male Yucatan minipigs and human tissue samples

isolated from the commercially available GenoSkin model. The total lipid fractions were accompanied by the differences in tissue viscoelasticity across the different locations, depth layers, and the two species. Our results agree with the previous work of Geerligs et al. on subcutaneous fat tissue of a Landrace pig [27]. Only the neck region showed far higher values of storage and loss moduli in our study. Also, it has been reported the porcine middle layer (in our case layer 2) is comparable to the deeper subcutaneous layer in the abdominal region of human skin tissues [27, 47]. This can be observed in our results in Figs. 4B and 7B, where the human samples are within $\sim \pm 0.5$ kPa range of the breast and belly layer 2. However, it can be observed the neck shows far higher moduli across all the tests.

The total lipid content across tissue locations, depths, and species was compared to see whether similarities in lipid content would be observed across samples that behaved similarly during rheological testing. In examining the total lipid content of minipig samples, we discovered the distribution of lipids remained relatively constant across layers in both the belly and neck tissues. On the other hand, significant differences in lipid content were observed across tissue layers in the minipig breast tissue, with the largest proportion occurring in the layer corresponding to the middle 2 mm of the original biopsy punch. These measurements correlated with histological findings illustrate that the neck and belly tissues share similar morphological characteristics, whereas the breast tissue contains a higher proportion of adipose and glandular deposits, particularly in the middle region. We observed that the human (female) SC had a higher proportion of total lipids compared to the male human samples. This agrees with prior findings indicating human female SC tissue tends to have higher numbers of adipocytes when compared to its male counterpart [48]. This clearly suggests biological sex and the presence of high levels of estrogen could be factors contributing to the recruitment of cell phenotypes that drive the accumulation of lipid material. When the lipid content of the minipig and human tissue samples was compared, the highest degree of similarity was observed between the minipig belly and neck samples and the male human samples. On the other hand, the lipid content of the human female SC was significantly different from nearly all minipig samples, except for layer 2 of the minipig breast and neck tissues. These groupings were also observed in the stress relaxation response (see "Stress Relaxation Tests" section) of the tissue samples. Taken altogether, these findings suggest the castrated male Yucatan minipig may serve as a better model for male human SC tissue rather than human female SC tissue. However, further study is required to understand the insights into female-specific studies, particularly regarding subcutaneous fat distribution and related rheological properties between female minipigs and human SCs.

Among the minipig tissues and their lipid contents, we observed a correlation coefficient of 0.73 with a statistical significance of 0.024 (See Fig. 6). However, the human SC cases were outliers and did not follow this trend. This can be observed in Fig. 6, where we see there is an overall increase in storage modulus (stiffness) as we increase lipid content in the tissues. But in the case of the human SC layers, especially the female case with 81.5% lipid mass, it has one of the lowest storage moduli. To explain these cases of inter-species exceptions, further quantification of fatty acid contents needs to be performed. Reports show that minipig lipids have a higher proportion of stearic and oleic fatty acids and less palmitic acid compared to human tissues [49, 50]. This affects the overall viscoelasticity as the fatty acid composition can alter the fluidity and packing of the lipids in the cell membrane, affecting the overall mechanical properties of the tissue [39, 51]. Stearic and oleic fatty acids are unsaturated fatty acids that increase the overall fluidity of the cell membrane, making it more flexible. This leads to a decrease in its elastic (storage) modulus, with an increase in the viscous (loss) modulus of the tissue [39, 40]. On the other hand, palmitic acid, which is a saturated fatty acid, makes the cell membrane more rigid, leading to an increase in bulk-elastic modulus and a decrease in the bulk-loss modulus of the tissue [39, 40]. Quantifications of the above-mentioned fatty acids would be required in developing a more detailed understanding of the biochemical cues for the observed bulk-viscoelastic behavior.

Moreover, additional intra-species exceptions can be observed in Fig. 4A, where $G'(\omega)$ for the minipig neck is higher as compared to its belly. However, the lipid fraction in the minipig and neck was quantified to be fairly similar (see Fig. 3B). Also, in the case of the minipig belly, despite having a similar lipid content (refer to Fig. 2D) in each layer, $G'(\gamma)$ and $G''(\gamma)$ had strong variations across each layer (See Figs. 7 and 12). The minipig neck (breast) showed the highest (lowest) storage modulus across all the rheological tests, especially in layer 1. The closest agreement in storage modulus, between all three minipig locations, was observed in layer 3. This indicates a stiffer tissue structure in the neck, which could provide more (i) resistance to needle penetration, (ii) increased injection force and resistance during needle insertion, (iii) possibly influence drug dispersion in shorter timescales post-injection [8, 9]. A similar trend was noted for the relaxation behavior. Neck tissues exhibited the longest relaxation times across all layers except for layer 2, indicating slower stress relaxation and more prolonged tissue deformation post-injection across the layer 1 and layer 2 across the neck region for the minipig. We observed that reduced strain-stiffening at high strain amplitudes is caused by higher lipid content within

the tissue. Additionally, the degree of strain-stiffening and shear-thinning was particularly pronounced in minipig belly and neck. Increased stiffening can increase the localized pressure and reduced distribution of the drug, impacting the absorption and efficacy, and elastic recovery of the tissue post-injection. This behavior needs to be considered when designing injection protocols and devices to ensure effective drug delivery and minimize discomfort and the chances of tissue damage. More importantly, tissue mechanical properties can be used in poroelastic models of tissue and study of drug absorption post SC injections [8–12].

Our study concludes the existence of species, anatomical location, tissue depth, sex, and strain-dependent rheological properties. The findings also suggest a male Yucatan minipig might present a better model for male human SC tissue, as compared to human female SC tissue. Hence, we expect the outcomes from this study to motivate future works, including studies on larger sample size and in avoiding generalization of the viscoelasticity for minipig-skin tissues over human SC tissues when used for comparison purposes. Hopefully, this will stimulate more detailed comparative studies on body location and depth-based analysis, exploring both the micro/macro-mechanical properties in relation to the biochemical cues.

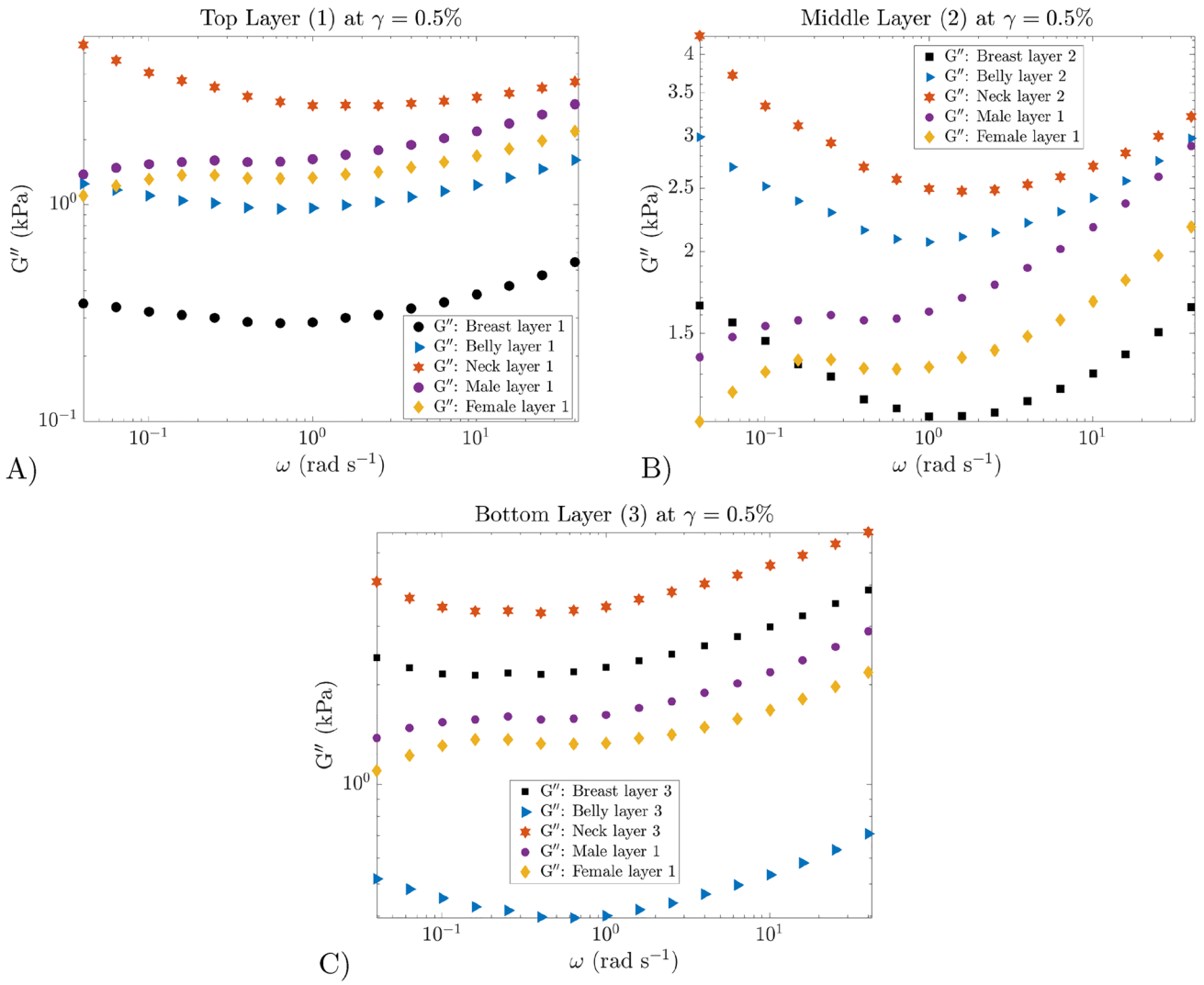

Fig. 11 Loss modulus, $G''(\omega)$, for the three different regions of the minipig, i.e., breast, belly, and neck, across the different layers, 1–3, represented through **A**–**C**, respectively. The male and female human SC samples are overlaid in all the figures for comparison. Manual scaling has been done for, $G''(\gamma)$, across **A**, **B**, and **C**, to make the breast, belly, and neck layers' magnitude differences decipherable. Standard deviations were about the size of the symbols

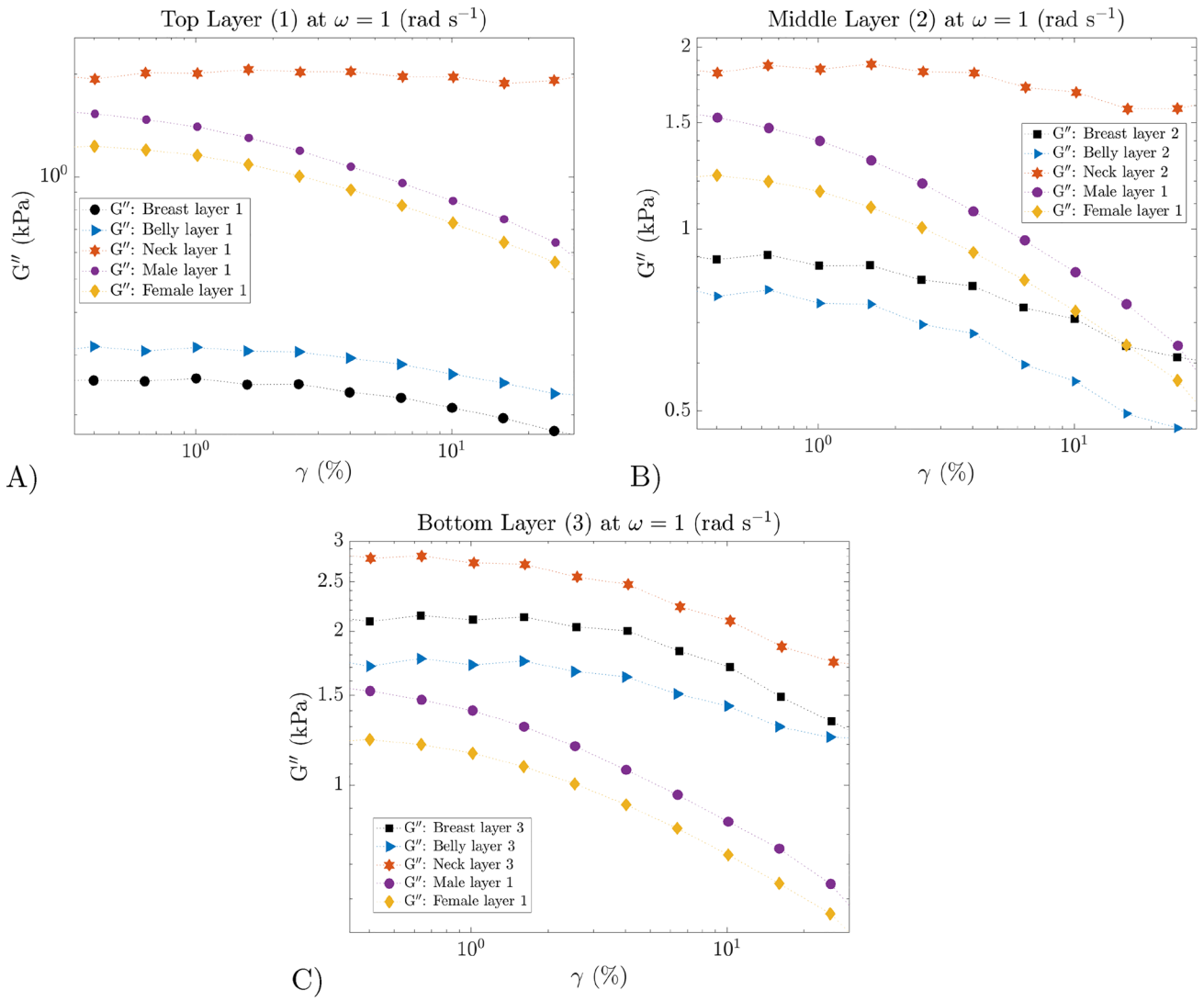

Fig. 12 Loss modulus, $G''(\gamma)$, for the three different regions of the minipig, i.e., breast, belly, and neck, across the different layers, 1–3, represented through **A–C**, respectively. The male and female human SC samples are overlaid in all the figures for comparison. Manual scaling has been done for, $G''(\gamma)$, across **A**, **B**, and **C**, to make the breast, belly, and neck layers' magnitude differences decipherable. An average variation of 16.5% was observed between the three triplicates. Continuous lines are overlaid in order to guide the reader and are not a fit

Table 1 Power-law fit for the storage modulus, $G'(\omega)$, for the various locations and layers

	Layer 1	Layer 2	Layer 3
Minipig breast			
$G'(1)$ (kPa)	1.480	6.565	10.280
p (–)	0.108	0.089	0.130
Minipig belly			
$G'(1)$ (kPa)	2.232	4.758	11.340
p (–)	0.098	0.107	0.098
Minipig neck			
$G'(1)$ (kPa)	23.050	16.470	16.21
p (–)	0.052	0.070	0.112
HM belly			
$G'(1)$ (kPa)	5.210	–	–
p (–)	0.142	–	–
HF belly			
$G'(1)$ (kPa)	4.283	–	–
p (–)	0.146	–	–

Table 2 Four-element Maxwell model fit on the stress relaxation behavior, $G(t)$, for all the three anatomical locations and depth layers

	Layer 1	Layer 2	Layer 3
Breast			
E_1 (kPa)	0.1039	0.4224	0.9387
E_2 (kPa)	0.1628	1.596	0.7168
E_3 (kPa)	0.1033	0.3774	1.3680
E_4 (kPa)	0.3496	0.4596	0.6396
λ_1 (s)	3.50	28.61	0.60
λ_2 (s)	0.57	879.80	3.64
λ_3 (s)	25.39	3.68	645.70
λ_4 (s)	789	0.59	25.00
Belly			
E_1 (kPa)	0.1639	0.8862	2.2660
E_2 (kPa)	0.2603	0.2843	1.1120
E_3 (kPa)	0.1747	0.3788	0.8563
E_4 (kPa)	0.5304	0.2863	0.8576
λ_1 (s)	27.07	723.60	675.70
λ_2 (s)	0.58	3.86	0.65
λ_3 (s)	3.62	0.61	4.02
λ_4 (s)	869.10	27.93	27.93
Neck			
E_1 (kPa)	2.0690	1.2580	0.8165
E_2 (kPa)	2.2320	4.3800	0.8492
E_3 (kPa)	7.0860	1.6400	1.1910
E_4 (kPa)	1.8330	1.2490	2.6470
λ_1 (s)	4.25	29.89	25.78
λ_2 (s)	0.68	697.10	3.59
λ_3 (s)	779.70	0.66	0.62
λ_4 (s)	35.52	4.01	667.80
HM belly			
E_1 (kPa)	0.7321	–	–
E_2 (kPa)	1.822	–	–
E_3 (kPa)	0.9219	–	–
E_4 (kPa)	3.144	–	–
λ_1 (s)	6.157	–	–
λ_2 (s)	572.8	–	–
λ_3 (s)	34.68	–	–
λ_4 (s)	0.6434	–	–
HF belly			
E_1 (kPa)	1.585	–	–
E_2 (kPa)	0.0782	–	–
E_3 (kPa)	2.399	–	–
E_4 (kPa)	0.8892	–	–
λ_1 (s)	1.417	–	–
λ_2 (s)	0.0046	–	–
λ_3 (s)	596.5	–	–
λ_4 (s)	20.12	–	–

Table 3 Relaxation half-life times, $\lambda_{1/2}$, for all the three anatomical locations and depth layers

	$\lambda_{1/2}$ (s)		
	Layer 1	Layer 2	Layer 3
Breast	48.7	186	25.4
Belly	71.8	84.9	57.1
Neck	165	120.5	164.5
Male	22.8	–	–
Female	55.1	–	–

Table 4 *S* and *T* parameters at $\gamma_1 = 15\%$ for all the samples tested

	Layer 1 (SC)		Layer 2		Layer 3	
	S	*T*	*S*	*T*	*S*	*T*
Breast	0.10	− 0.17	0.16	− 0.23	0.10	− 0.25
Belly	0.18	− 0.29	0.24	− 0.43	0.16	− 0.07
Neck	0.18	− 0.24	0.17	− 0.23	0.17	− 0.29
HM belly	0.02	− 0.11	–	–	–	–
HF belly	0.15	− 0.09	–	–	–	–

HM/HF belly represents male human/female belly, respectively

Table 5 *S* and *T* parameters at $\gamma_1 = 40\%$ for all the samples tested

	Layer 1 (SC)		Layer 2		Layer 3	
	S	*T*	*S*	*T*	*S*	*T*
Breast	0.25	− 0.57	0.38	− 0.43	0.19	− 0.45
Belly	0.45	− 1.2	0.57	− 1.48	0.41	− 0.59
Neck	0.45	− 0.91	0.42	− 0.87	0.35	− 0.45
HM belly	0.17	− 0.35	–	–	–	–
HF belly	0.03	− 0.47	–	–	–	–

HM/HF belly represents male human/female belly, respectively

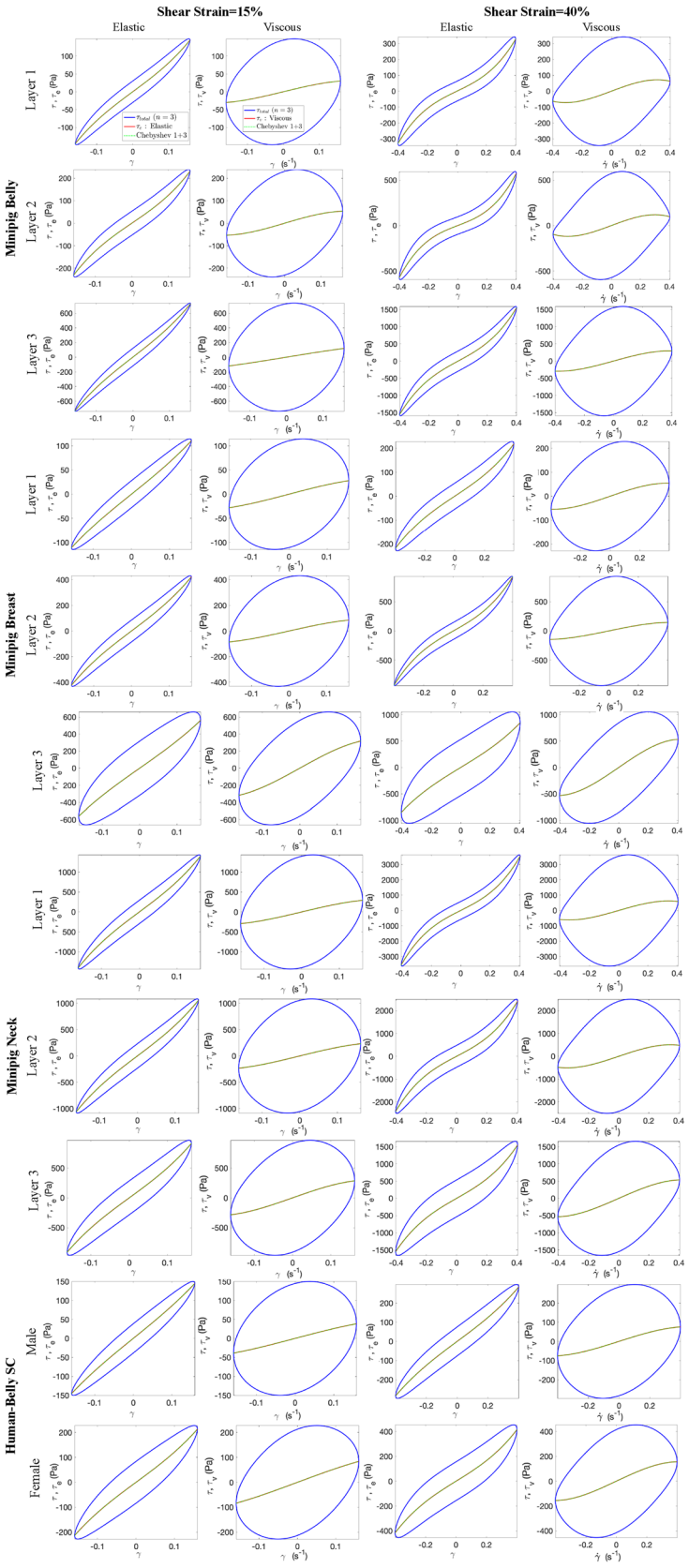

Fig. 13 LB curves plotted using MITLaos of all the tissues at 15% and 40% shear-strain amplitudes. The blue (red) continuous curves are for the total stress (elastic/viscous) filtered for the 3rd harmonic. The area enclosed by the LB curves is related to the energy dissipated per unit volume in one complete cycle of the oscillatory strain. The legend shown in the case for the elastic behavior of the minipig belly layer 1 at 15% strain is the same for all the figures

Appendix 1: Rheological Data Fit Parameters

The loss modulus from the frequency and amplitude sweeps is represented in Figs. 11 and 12, respectively. The results of the power-law and GM model fit are presented in Tables 1 and 2, respectively. Relaxation half-life times for all the tissues are shown in Table 3.

Appendix 2: LAOS

The degree of elastic and viscous non-linearities is quantified in Tables 4 and 5, respectively. The LB curves for the two strains, 15% and 40%, are illustrated for all the cases in Fig. 13. The increased distortions at 40% strain in Fig. 13 reveal a strong non-linear response.

Acknowledgements This research was supported by a grant from Eli Lilly and Company. The authors would also like to thank Jordanna M. Payne for her assistance in acquiring the tissue samples and Randy Ewoldt for providing the MITlaos software.

Declarations

Conflict of interest No benefits in any form have been or will be received from a commercial party related directly or indirectly to the subject of this manuscript.

References

1. Dychter, S. S., D. A. Gold, and M. F. Haller. Subcutaneous drug delivery: a route to increased safety, patient satisfaction, and reduced costs. *J. Infus. Nurs.* 35(3):154–160, 2012.
2. Stoner, K. L., H. Harder, L. J. Fallowfield, and V. A. Jenkins. Intravenous versus subcutaneous drug administration. Which do patients prefer? A systematic review. *Patient Patient Centered Outcomes Res.* 8:145–153, 2015.
3. Mathias, N., S. Huille, M. Picci, R. P. Mahoney, R. J. Pettis, B. Case, B. Helk, D. Kang, R. Shah, J. Ma, *et al.* Towards more tolerable subcutaneous administration: review of contributing factors for improving combination product design. *Adv. Drug Deliv. Rev.*209:115301, 2024.
4. Turner, M. R., and S. V. Balu-Iyer. Challenges and opportunities for the subcutaneous delivery of therapeutic proteins. *J. Pharm. Sci.* 107(5):1247–1260, 2018.
5. Viola, M., J. Sequeira, R. Seiça, F. Veiga, J. Serra, A. C. Santos, and A. J. Ribeiro. Subcutaneous delivery of monoclonal antibodies: how do we get there? *J. Control. Release*. 286:301–314, 2018.
6. Sequeira, J. A., A. C. Santos, J. Serra, C. Estevens, R. Seiça, F. Veiga, and A. J. Ribeiro. Subcutaneous delivery of biotherapeutics: challenges at the injection site. *Expert Opin. Drug Deliv.* 16(2):143–151, 2019.
7. Guo, X., and W. Wang. Challenges and recent advances in the subcutaneous delivery of insulin. *Expert Opin. Drug Deliv.* 14(6):727–734, 2017.
8. Rahimi, E., H. Gomez, and A. M. Ardekani. Transport and distribution of biotherapeutics in different tissue layers after subcutaneous injection. *Int. J. Pharm.* 626:122125, 2022.
9. Rahimi, E., S. Aramideh, D. Han, H. Gomez, and A. M. Ardekani. Transport and lymphatic uptake of monoclonal antibodies after subcutaneous injection. *Microvasc. Res.* 139:104228, 2022.
10. Han, D., E. Rahimi, S. Aramideh, and A. M. Ardekani. Transport and lymphatic uptake of biotherapeutics through subcutaneous injection. *J. Pharm. Sci.* 111(3):752–768, 2022.
11. Lucio, M., Y. Leng, H. Wang, A. M. Ardekani, P. P. Vlachos, G. Shi, and H. Gomez. Computational modeling of the effect of skin pinch and stretch on subcutaneous injection of monoclonal antibodies using autoinjector devices. *Biomech. Model. Mechanobiol.* 22(6):1965–1982, 2023.
12. Lucio, M., Y. Leng, A. Hans, I. Bilionis, M. Brindise, A. M. Ardekani, P. P. Vlachos, and H. Gomez. Modeling large-volume subcutaneous injection of monoclonal antibodies with anisotropic porohyperelastic models and data-driven tissue layer geometries. *J. Mech. Behav. Biomed. Mater.* 138:105602, 2023.
13. Zhong, X., H. Mitra, J.-C. Veilleux, E. Simmons, G. H. Shi, and A. M. Ardekani. The role of liquid rheological properties on the injection process of a spring-driven autoinjector. *Int. J. Pharm.* 628:122296, 2022.
14. Singh, V. K., K. D. Thrall, and M. Hauer-Jensen. Minipigs as models in drug discovery. *Expert Opin. Drug Discov.* 11(12):1131–1134, 2016.
15. Gibney, M. A., C. H. Arce, K. J. Byron, and L. J. Hirsch. Skin and subcutaneous adipose layer thickness in adults with diabetes at sites used for insulin injections: implications for needle length recommendations. *Curr. Med. Res. Opin.* 26(6):1519–1530, 2010.
16. Everett, J. S., and M. S. Sommers. Skin viscoelasticity: physiologic mechanisms, measurement issues, and application to nursing science. *Biol. Res. Nurs.* 15(3):338–346, 2013.
17. Li, D., P. A. Janmey, and R. G. Wells. Local fat content determines global and local stiffness in livers with simple steatosis. *FASEB Bioadv.* 5(6):251–261, 2022.
18. Abuhattum, S., P. Kotzbeck, R. Schlüßler, A. Harger, A. Schellenberger, K. Kim, J.-C. Escolano, T. Müller, J. Braun, M. Wabitsch, *et al.* Adipose cells and tissues soften with lipid accumulation while in diabetes adipose tissue stiffens. *Sci. Rep.* 12(1):1–17, 2022.
19. Ludescher, B., M. Rommel, T. Willmer, A. Fritsche, F. Schick, and J. Machann. Subcutaneous adipose tissue thickness in adults-correlation with bmi and recommendations for pen needle lengths for subcutaneous self-injection. *Clin. Endocrinol.* 75(6):786–790, 2011.
20. Usach, I., R. Martinez, T. Festini, and J.-E. Peris. Subcutaneous injection of drugs: literature review of factors influencing pain sensation at the injection site. *Adv. Ther.* 36:2986–2996, 2019.
21. Lozano, P. F., M. Scholze, C. Babian, H. Scheidt, F. Vielmuth, J. Waschke, B. Ondruschka, and N. Hammer. Water-content related alterations in macro and micro scale tendon biomechanics. *Sci. Rep.* 9(1):1–12, 2019.
22. Andersson, I., and A. Hedvall. Relationships between skin properties and body water level. Master of Science Thesis in Medical Engineering, Stockholm, 2013.
23. Hammer, N., D. Huster, S. Fritsch, C. Hädrich, H. Koch, P. Schmidt, F. Sichting, M.F.-X. Wagner, and A. Boldt. Do cells contribute to tendon and ligament biomechanics? *PLoS ONE.* 9(8):105037, 2014.
24. Malhotra, D., S. Pan, L. Rüther, T. B. Goudoulas, G. Schlippe, W. Voss, and N. Germann. Linear viscoelastic and microstructural properties of native male human skin and in vitro 3d reconstructed skin models. *J. Mech. Behav. Biomed. Mater.* 90:644–654, 2019.
25. Pan, S., D. Malhotra, and N. Germann. Nonlinear viscoelastic properties of native male human skin and in vitro 3d reconstructed skin models under laos stress. *J. Mech. Behav. Biomed. Mater.* 96:310–323, 2019.

26. Sun, Z., S.-H. Lee, B. D. Gepner, J. Rigby, J. J. Hallman, and J. R. Kerrigan. Comparison of porcine and human adipose tissue loading responses under dynamic compression and shear: A pilot study. *J. Mech. Behav. Biomed. Mater.* 113:104112, 2021.
27. Geerligs, M., G. W. Peters, P. A. Ackermans, C. W. Oomens, and F. Baaijens. Linear viscoelastic behavior of subcutaneous adipose tissue. *Biorheology*. 45(6):677–688, 2008.
28. Corder, R. D., S. V. Gadi, R. B. Vachieri, F. L. Jayes, J. M. Cullen, S. A. Khan, and D. K. Taylor. Using rheology to quantify the effects of localized collagenase treatments on uterine fibroid digestion. *Acta Biomater.* 134:443–452, 2021.
29. Corder, R. D., R. B. Vachieri, M. E. Martin, D. K. Taylor, J. M. Fleming, and S. A. Khan. Linear and nonlinear rheology of liberase-treated breast cancer tumors. *Biomaterials Science*. 11(6):2186–2199, 2023.
30. Madsen, C. D., and T. R. Cox. Relative stiffness measurements of tumour tissues by shear rheology. *Bio-Protoc.* 7(9):2265–2265, 2017.
31. Polio, S. R., A. N. Kundu, C. E. Dougan, N. P. Birch, D. E. Aurian-Blajeni, J. D. Schiffman, A. J. Crosby, and S. R. Peyton. Cross-platform mechanical characterization of lung tissue. *PLoS ONE*. 13(10):0204765, 2018.
32. Tanner, R. I. Engineering Rheology. Oxford: OUP, 2000.
33. Pipkin, A. C. Lectures on Viscoelasticity Theory. New York: Springer, 2012.
34. Roylance, D. *Engineering Viscoelasticity*. Cambridge: Department of Materials Science and Engineering, Massachusetts Institute of Technology, pp. 1–37, 2001.
35. Ewoldt, R. H., A. Hosoi, and G. H. McKinley. New measures for characterizing nonlinear viscoelasticity in large amplitude oscillatory shear. *J. Rheol.* 52(6):1427–1458, 2008.
36. Ewoldt, R.H.: Nonlinear viscoelastic materials: Bioinspired applications and new characterization measures. PhD thesis, Massachusetts Institute of Technology (2009)
37. Eg, B., and D. Wj. A rapid method of total lipid extraction and purification. *Can. J. Biochem. Physiol.* 37(8):911–917, 1959.
38. Bovo, S., A. Di Luca, G. Galimberti, S. Dall'Olio, and L. Fontanesi. A comparative analysis of label-free liquid chromatography-mass spectrometry liver proteomic profiles highlights metabolic differences between pig breeds. *PLoS ONE*. 13(9):0199649, 2018.
39. Kaviarasan, K., M. Arjunan, and K. Pugalendi. Lipid profile, oxidant-antioxidant status and glycoprotein components in hyperlipidemic patients with/without diabetes. *Clin. Chim. Acta*. 362(1–2):49–56, 2005.
40. Yang, X., W. Sheng, G. Y. Sun, and J.C.-M. Lee. Effects of fatty acid unsaturation numbers on membrane fluidity and α-secretase-dependent amyloid precursor protein processing. *Neurochem. Int.* 58(3):321–329, 2011.
41. Tan, K., S. Cheng, L. Jugé, and L. E. Bilston. Characterising soft tissues under large amplitude oscillatory shear and combined loading. *J. Biomech.* 46(6):1060–1066, 2013.
42. Chan, R. W. Nonlinear viscoelastic characterization of human vocal fold tissues under large-amplitude oscillatory shear (laos). *J. Rheol.* 62(3):695–712, 2018.
43. Hyun, K., M. Wilhelm, C. O. Klein, K. S. Cho, J. G. Nam, K. H. Ahn, S. J. Lee, R. H. Ewoldt, and G. H. McKinley. A review of nonlinear oscillatory shear tests: Analysis and application of large amplitude oscillatory shear (laos). *Prog. Polym. Sci.* 36(12):1697–1753, 2011.
44. Chaudhuri, O., L. Gu, D. Klumpers, M. Darnell, S. A. Bencherif, J. C. Weaver, N. Huebsch, H.-P. Lee, E. Lippens, G. N. Duda, *et al.* Hydrogels with tunable stress relaxation regulate stem cell fate and activity. *Nat. Mater.* 15(3):326–334, 2016.
45. Nicolle, S., J. Decorps, B. Fromy, and J.-F. Palierne. New regime in the mechanical behavior of skin: strain-softening occurring before strain-hardening. *J. Mech. Behav. Biomed. Mater.* 69:98–106, 2017.
46. Capilnasiu, A., L. Bilston, R. Sinkus, and D. Nordsletten. Nonlinear viscoelastic constitutive model for bovine liver tissue. *Biomech. Model. Mechanobiol.* 19:1641–1662, 2020.
47. Paus, R., J. Klein, P. Permana, M. Owecki, G. Chaldakov, M. Böhm, G. Hausman, C. Lapière, P. Atanassova, J. Sowiński, *et al.* What are subcutaneous adipocytes really good for...? *Exp. Dermatol.* 16(1):45–47, 2007.
48. Andersson, D., E. Arner, D. Hogling, M. Ryden, and P. Arner. Abdominal subcutaneous adipose tissue cellularity in men and women. *Int. J. Obes.* 41(10):1564–1569, 2017.
49. Brockerhoff, H., and M. Yurkowski. Stereospecific analyses of several vegetable fats. *J. Lipid Res.* 7(1):62–64, 1966.
50. Douglas, W. R. Of pigs and men and research: a review of applications and analogies of the pig, *Sus scrofa*, in human medical research. *Space Life Sci.* 3(3):226–234, 1972.
51. Alkhouli, N., J. Mansfield, E. Green, J. Bell, B. Knight, N. Liversedge, J. C. Tham, R. Welbourn, A. C. Shore, K. Kos, *et al.* The mechanical properties of human adipose tissues and their relationships to the structure and composition of the extracellular matrix. *Am. J. Physiol. Endocrinol. Metab.* 305(12):1427–1435, 2013.